Electronic Supporting Information

Magnetic Field and Dilution Effects on the Slow Relaxation of $\{Er_3\}$ Triangles Based Arsenotungstate Single-Molecule Magnet

Hanhan Chen,[a] Lin Sun,[a] Jinpeng Zhang,[a] Zikang, Xiao,[a] Pengtao Ma,*[a] Jingping Wang,[a] Yiquan Zhang*[b] and Jingyang Niu*[a]

[a]*Henan Key Laboratory of Polyoxometalate Chemistry, College of Chemistry and Chemical Engineering, Henan University, Kaifeng, Henan 475004, P. R. China*
[b]*Jiangsu Key Laboratory for NSLSCS, School of Physical Science and Technology, Nanjing Normal University, Nanjing 210023, China. E-mail: zhangyiquan@njnu.edu.cn.*

Fig. S3. EDX spectra of **1** and **Er@2** show the presence of C, O, As, K, W, Er and Y element in the lattice. The measured ratios of Er^{3+}/ Y^{3+} ions are almost consistent with nominal ratios.

Fig. S4. Frequency dependence of the in-phase (χ_M'-*T*) and out-of-phase (χ_M'') products under a zero dc field for **1**. The lines are guides to the eyes.

Fig. S5. At 2.0 K, sweep field diagram of **1** from 0 to 5000 Oe, and the optimal dc field was determined to be 1500 Oe at 2.0 K, 707.2Hz.

Fig. S6. At 2.0 K, the real part (left) and imaginary part (right) of compound **1** ac signal frequency dependence diagram, solid line represents Debye model fitting curve, fitting parameters: α_1= 0.16421; α_2= 0.39146; τ_1= 2.22884×10^{-4} s; τ_2= 0.24782 s; $\chi_{s,tot}$= 11.01469 cm^3 mol^{-1}; $\Delta\chi_1$= 4.66775 cm^3 mol^{-1}; $\Delta\chi_2$= 8.76193 cm^3 mol^{-1}.

Fig. S7. At 2.1 K, the real part (left) and imaginary part (right) of compound **1** ac signal frequency dependence diagram, solid line represents Debye model fitting curve, fitting parameters: α_1= 0.18020; α_2= 0.38504; τ_1= 1.81589×10^{-4} s; τ_2= 0.19757 s; $\chi_{s,tot}$= 10.61995 cm^3 mol^{-1}; $\Delta\chi_1$= 4.62245 cm^3 mol^{-1}; $\Delta\chi_2$= 7.62994 cm^3 mol^{-1}.

Fig. S8. At 2.2 K, the real part (left) and imaginary part (right) of compound **1** ac signal frequency dependence diagram, solid line represents Debye model fitting curve, fitting parameters: α_1= 0.23469; α_2= 0.21989; τ_1= 1.48248×10^{-4} s; τ_2= 0.16258 s; $\chi_{s,tot}$= 10.16743 cm^3 mol^{-1}; $\Delta\chi_1$= 4.97757 cm^3 mol^{-1}; $\Delta\chi_2$= 4.31230 cm^3 mol^{-1}.

Fig. S9. At 2.4 K, the real part (left) and imaginary part (right) of compound **1** ac signal frequency dependence diagram, solid line represents Debye model Fitting curve, fitting parameters: α_1=0.2878; α_2= 0.22097; τ_1= 1.00191×10^{-4} s; τ_2= 0.10621 s; $\chi_{s,tot}$= 9.67703 cm^3 mol^{-1}; $\Delta\chi_1$= 5.03636 cm^3 mol^{-1}; $\Delta\chi_2$= 3.30812 cm^3 mol^{-1}.

Fig. S10. At 2.6 K, the real part (left) and imaginary part (right) of compound **1** ac signal frequency dependence diagram, solid line represents Debye model fitting curve, fitting parameters: α_1= 0.28777; α_2= 0.27865; τ_1= 7.99563×10^{-5} s; τ_2= 0.08430 s; $\chi_{s,tot}$= 9.66670 cm^3 mol^{-1}; $\Delta\chi_1$= 4.44723 cm^3 mol^{-1}; $\Delta\chi_2$= 3.11013 cm^3 mol^{-1}.

Fig. S11. At 2.8 K, the real part (left) and imaginary part (right) of compound **1** ac signal frequency dependence diagram, solid line represents Debye model fitting curve, fitting parameters: α_1= 0.37304; α_2= 0.28301; τ_1= 3.58979×10^{-5} s; τ_2= 0.06086 s; $\chi_{s,tot}$= 9.14171 cm^3 mol^{-1}; $\Delta\chi_1$= 4.05652 cm^3 mol^{-1}; $\Delta\chi_2$= 2.01895 cm^3 mol^{-1}.

Fig. S12. At 3.0 K, the real part (left) and imaginary part (right) of compound **1** ac signal frequency dependence diagram, solid line represents Debye model fitting curve, fitting parameters: α_1= 0.42971; α_2= 0.18214; τ_1= 2.33217×10^{-5} s; τ_2= 0.04121 s; $\chi_{s,tot}$= 7.511220 cm^3 mol^{-1}; $\Delta\chi_1$= 6.29960 cm^3 mol^{-1}; $\Delta\chi_2$= 1.61919 cm^3 mol^{-1}.

Fig. S13. At 3.2 K, the real part (left) and imaginary part (right) of compound **1** ac signal frequency dependence diagram, solid line represents Debye model fitting curve, fitting parameters: α_1= 0.45949; α_2= 0.23169; τ_1= 9.37751×10^{-6} s; τ_2= 0.0295 s; $\chi_{s,tot}$= 7.35975 cm^3 mol^{-1}; $\Delta\chi_1$= 5.3805 cm^3 mol^{-1}; $\Delta\chi_2$= 1.32714 cm^3 mol^{-1}.

Fig. S14. Plot of ln(τ/*s*) versus T^{-1} for compound **1** under 1500 dc field. Left: FR process, right: SR process.

Fig. S15. Frequency dependence of the in-phase (χ_M'*T*) and out-of-phase (χ_M'') products under a zero dc field for **Er@2**.

Fig. S16. Cole–Cole plot under a zero dc field for **Er@2** at the indicated temperatures. The lines are guides to the eyes.

Fig. S17. Plot of ln(τ/s) versus T^{-1} of **Er@2** under a zero dc field with fitting results.
Fig. S18. Frequency dependence of the in-phase (χ_M') and out-of-phase (χ_M'') products under an optimized 1500 Oe dc field for **Er@2**. The lines are guides to the eyes.
Fig. S19. plot of ln(τ/*s*) versus T^{-1} for compound **Er@2** under 1500 dc field.
Fig. S20. Magnetization blocking barriers of individual Er^{3+} fragments from compound **1**.
Fig. S21. Scheme of the Er^{3+}-Er^{3+} interactions in compound **1**.
Fig. S22. Calculated (red solid line) and experimental (white circle) data of magnetic susceptibility of {Er_3} fragment in **1**. The intermolecular interaction zJ' of {Er_3} fragment in **1** was fitted to -0.16 cm^{-1}.
Fig. S23. Calculated orientations of the local main magnetic axes on Er^{3+} ions of {Er_3} fragment in **1** in the ground KDs.
Fig. S24. Calculated model structures of individual Er^{3+} fragments in **1**; H atoms are omitted for clarify.

Material and physical measurements

All other chemicals were commercially purchased and used without further purification. The potassium salt of the dilacunary $K_{14}[As_2W_{19}O_{67}(H_2O)]$ precursor was synthesized according to the reported literature[S1] and confirmed by IR spectrum. IR spectra of all compounds were recorded on a Bruker VERTEX 70 IR spectrometer using KBr pellets in the range of 4000–400 cm^{-1}. (Figure S1) Elemental analyses (C, H) were conducted on a Perkin-Elmer 2400-II CHNS/O analyzer. ICP analyses were performed on a PerkinElmer Optima 2000 ICP–OES spectrometer. (Table S10) Thermogravimetric analysis (TGA) analyses were performed on a NETZSCH STA 449 F5 Jupiter thermal analyzer in flowing N_2 with a heating rate of 10 °C min^{-1} (Figure S2). EDX measurements were recorded on a JSM-7610F scanning electron microscope with an OXFORD x-act EDS system (Figure S3). Variable-temperature magnetic susceptibility data were obtained on a SQUID magnetometer (Quantum Design, MPMS3) in the temperature range of 2–300 K.

X-ray Crystallography

Excellent single crystals of the three compounds were stilled in a capillary tube when prepared for data collection at 150(2) K as they weather easily. Indexing and data collection were performed on a Bruker D8 VENTURE PHOTON II diffractometer with Mo Kα radiation (λ = 0.71073 Å). Direct methods successfully located the tungsten atoms, and successive Fourier syntheses revealed the remaining atoms. Refinements were done by full-matrix least-squares on F^2 using the SHELXL-2018 program suite for all data.[S2] In the final refinement, almost all the

atoms except few water O atoms were refined anisotropically; the disordered K countercations and few O atoms were refined isotropically. The hydrogen atoms of the malate groups were placed in calculated positions and then refined using a riding model. All H atoms on water molecules were directly included in the molecular formula.

Computational details

For three-dimensional cluster of compound **1**, we extracted a three-core unit including three types of individual Er^{3+} fragments indicated as **Er1**, **Er2** and **Er3**. Complete-active-space self-consistent field (CASSCF) calculations on three types of individual Er^{3+} fragments from complex **1** (see Figure S24 for the calculated model structures) on the basis of single-crystal X-ray determined geometry have been carried out with MOLCAS 8.4[S3] program package. Each individual Er^{3+} fragment was calculated keeping the experimentally determined structure of the corresponding compound while replacing the nearest neighboring Er^{3+} ions by diamagnetic Lu^{3+}, and the influence of the other surrounding W^{6+} ions were taken into account by the closed-shell Ba^{2+} *ab initio* embedding model potentials (AIMP; Ba.ECP.Pascual.0s.0s.0e-AIMP-BaF2.).[S4]

The basis sets for all atoms are atomic natural orbitals from the MOLCAS ANO-RCC library: ANO-RCC-VTZP for Er^{3+}; VTZ for close O; VDZ for distant atoms. The calculations employed the second order Douglas-Kroll-Hess Hamiltonian, where scalar relativistic contractions were taken into account in the basis set and the spin-orbit couplings were handled separately in the restricted active space state interaction (RASSI-SO) procedure. For individual Er^{3+} fragment, active electrons in 7 active spaces include all *f* electrons (CAS(11 in 7 for Er^{3+})) in the CASSCF calculation. To exclude all the doubts, we calculated all the roots in the active space. We have mixed the maximum number of spin-free state which was possible with our hardware (all from 35 quadruplets, all from 112 doublets). SINGLE_ANISO[S5] program was used to obtain energy levels, ***g*** tensors, magnetic axes, *et al.,* based on the above CASSCF/RASSI-SO calculations.

To fit the exchange interactions between Er^{3+} ions in compound **1**, we took two steps to obtain them. Firstly, we calculated individual Er^{3+} fragments using CASSCF/RASSI-SO to obtain the corresponding magnetic properties. Then, the exchange interactions between the magnetic centers were considered within the Lines model,[S6] while the account of the dipole-

dipole magnetic couplings were treated exactly. The Lines model is effective and has been successfully used widely in the research field of *d* and *f*-elements SMMs.[S7]

The Ising exchange Hamiltonian for **1** is:

$$\hat{H}_{exch} = -J_1 \hat{S}_{Er1} \hat{S}_{Er2} - J_2 \hat{S}_{Er1} \hat{S}_{Er3} - J_3 \hat{S}_{Er2} \hat{S}_{Er3} \quad (1)$$

The J_{total} is the parameter of the total magnetic interaction ($J_{total} = J_{dip} + J_{exch}$) between magnetic center ions. The $\tilde{S}_{Er}$ = 1/2 is the ground pseudospin on Er^{3+} sites. The dipolar magnetic coupling can be calculated exactly, while the exchange coupling constants were fitted through comparison of the computed and measured magnetic susceptibilities using the POLY_ANISO program.[S7]

Table S1. Crystallographic data and structure refinements for **1**, **2** and **Er@2**.

	1	**2**	**Er@2**
Empirical formula	$C_8H_6As_4Er_6K_{18}O_{210}W_{38}$	$C_8H_6As_4K_{16}O_{208}W_{38}Y_6$	$C_8H_6As_4Er_{0.3}K_{20}O_{219}W_{38}Y_{5.7}$
Formula weight	12455.47	11875.17	12231.07
Temperature / K	150(2)	150(2)	150(2)
Crystal system	Monoclinic	monoclinic	monoclinic
Space group	*P*2(1)/*n*	*P*2(1)/*n*	*P*2(1)/*n*
a [Å]	20.6656(19)	20.6656(19)	20.520(3)
b [Å]	25.056(2)	25.056(2)	24.926(4)
c [Å]	22.596(2)	22.596(2)	22.516(3)
β [°]	112.570(4)	112.570(4)	112.644(4)
V [Å^3]	10804.1(17)	10804.1(17)	10629(3)
Z	2	2	2
ρ_{calcd} [g cm^{-3}]	3.829	3.650	3.822
μ [mm^{-1}]	23.504	22.753	23.250
F(000)	10856.0	10400.0	10745.0
Index ranges	–24≤ h ≤ 21 -27≤ k ≤ 29 –26≤ l ≤ 26	–24≤ h ≤ 24 -29≤ k ≤ 29 –23≤ l ≤ 26	–24≤ h ≤ 23 -29≤ k ≤ 29 –26≤ l ≤ 26
Reflections collected	73900	122877	107923
Independent reflections	19179 [R_{int} = 0.0385]	19174 [R_{int} = 0.0745]	18904 [R_{int} = 0.0559]
data/restraints/parameters	19179/ 18/ 1257	19174/ 30/ 1243	18904/ 42/ 1360
Goodness-of-fit on F^2	1.043	1.017	1.038

R_1, wR_2 [$I > 2\sigma(I)$]		0.0348, 0.0821	0.0394, 0.0988	0.0305, 0.0713
R_1, wR_2 [all data]		0.0412, 0.0849	0.0497, 0.1045	0.0372, 0.0744
Largest Peak/hole/e Å^{-3}	diff.	3.71/-1.96	3.35/-2.87	3.26/-1.95

Table S2 BVS values for Er, As, and W atoms in **1**.

Atoms	BVS value	Atoms	BVS value	Atoms	BVS value
Er1	3.08	W4	6.18	W12	6.23
Er2	3.19	W5	6.16	W13	6.33
Er3	3.20	W6	6.21	W14	6.27
As1	2.97	W7	6.10	W15	6.06
As2	3.01	W8	5.96	W16	6.16
W1	6.09	W9	6.21	W17	5.95
W2	6.13	W10	6.27	W18	6.27
W3	6.41	W11	6.13	W19	6.24

Table S3 Possible geometries of nine coordinated metal centers.

geometry	point group	polyhedron
EP-9	D_{9h}	Enneagon
OPY-9	C_{8v}	Octagonal pyramid
HBPY-9	D_{7h}	Heptagonal bipyramid
JTC-9	C_{3v}	Johnson triangular cupola J3
JCCU-9	C_{4v}	Capped cube J8
CCU-9	C_{4v}	Spherical-relaxed capped cube
JCSAPR-9	C_{4v}	Capped square antiprism J10
CSAPR-9	C_{4v}	Spherical capped square antiprism
JTCTPR-9	D_{3h}	Tricapped trigonal prism J51
TCTPR-9	D_{3h}	Spherical tricapped trigonal prism
JTDIC-9	C_{3v}	Tridiminished icosahedron J63
HH-9	C_{2v}	Hula-hoop
MFF-9	Cs	Muffin

Table S4 Deviation parameters calculated by SHAPE from each ideal polyhedron for Er1.

	Er1
EP-9	37.187
OPY-9	21.858
HBPY-9	19.340
JTC-9	15.716
JCCU-9	10.750
CCU-9	9.840
JCSAPR-9	1.437
CSAPR-9	0.640
JTCTPR-9	2.170
TCTPR-9	1.090

JTDIC-9	12.444
HH-9	10.886
MFF-9	0.730

Table S5 Possible geometries of eight coordinated metal centers.

geometry	point group	polyhedron
OP-8	D_{8h}	Octagon
HPY-8	C_{7v}	Heptagonal pyramid
HBPY-8	D_{6h}	Hexagonal bipyramid
CU-8	O_h	Cube
SAPR-8	D_{4d}	Square antiprism
TDD-8	D_{2d}	Triangular dodecahedron
JGBF-8	D_{2d}	Johnson gyrobifastigium (J26)
JETBPY-8	D_{3h}	Johnson elongated triangular bipyramid (J14)
JBTPR-8	C_{2v}	Biaugmented trigonal prism (J50)
BTPR-8	C_{2v}	Biaugmented trigonal prism
JSD-8	D_{2d}	Snub diphenoid(J84)
TT-8	T_d	Triakis tetrahedron
ETBPY-8	D_{3h}	Elongated trigonal bipyramid

Table S6 Deviation parameters calculated by SHAPE from each ideal polyhedron for Er2 and Er3.

	Er2	Er3
OP-8	27.278	28.549
HPY-8	23.199	22.767
HBPY-8	15.383	16.065
CU-8	9.424	9.903
SAPR-8	0.648	0.742
TDD-8	2.773	1.395
JGBF-8	13.806	14.903
JETBPY-8	25.459	27.647
JBTPR-8	3.195	1.438

BTPR-8	2.504	1.148
JSD-8	5.545	3.674
TT-8	10.219	10.732
ETBPY-8	21.226	23.559

Table S7 Selected bond lengths (Å) of **1**.

Bond	Length	Bond	Length	Bond	Length
Er1-O28	2.568(8)	Er2-O27	2.279(8)	Er3-O30	2.265(8)
Er1-O32	2.353(8)	Er2-O32	2.301(8)	Er3-O33	2.303(7)
Er1-O33	2.340(8)	Er2-O62	2.319(8)	Er3-O68	2.308(8)
Er1-O63	2.605(8)	Er2-O63	2.484(8)	Er3-O72	2.342(9)
Er1-O64	2.308(8)	Er2-O1W	2.383(7)	Er3-O1W	2.456(7)
Er1-O1W	2.328(7)	Er2-O4W	2.352(8)	Er3-O7W	2.393(8)
Er1-O2W	2.377(8)	Er2-O5W	2.409(9)	Er3-O8W	2.393(8)
Er1-O3W	2.400(8)	Er2-O6W	2.330(8)	Er3-O9W	2.381(8)
Er1-O8W	2.506(7)				

Table S8 Selected bond angles (°) of **1**.

Bond	Angel	Bond	Angel
O28-Er1-O63	124.6(2)	O48-Er3-O56	75.330(15)
O32-Er1-O28	63.2(3)	O30-Er3-O56	145.274(22)
O32-Er1-O63	69.6(3)	O74-Er3-O56	121.051(17)
O32-Er1-O2W	134.1(3)	O8W-Er3-O56	79.343(15)
O32-Er1-O3W	82.9(3)	O7W-Er3-O56	74.347(14)
O32-Er1-O8W	137.2(3)	O6W-Er3-O56	74.599(14)
O33-Er1-O28	62.6(3)	O30-Er3-O48	139.355(18)
O33-Er1-O32	82.9(3)	O74-Er3-O48	72.278(13)
O33-Er1-O63	137.7(3)	O8W-Er3-O48	85.101(13)
O33-Er1-O2W	84.7(3)	O7W-Er3-O48	117.036(15)
O33-Er1-O3W	136.1(3)		
O33-Er1-O8W	67.4(3)		
O64-Er1-O28	139.1(3)		
O64-Er1-O32	139.5(3)		
O64-Er1-O33	134.9(3)		
O64-Er1-O63	71.1(3)		
O64-Er1-O1W	102.8(3)		
O64-Er1-O2W	73.9(3)		
O64-Er1-O3W	76.7(3)		
O64-Er1-O8W	68.8(3)		
O1W-Er1-O28	117.9(3)		
O1W-Er1-O32	72.1(3)		
O1W-Er1-O33	71.5(3)		

O1W-Er1-O63	69.7(2)		
O1W-Er1-O2W	142.7(3)		
O1W-Er1-O3W	140.5(3)		
O1W-Er1-O8W	69.7(2)		
O2W-Er1-O28	71.9(3)		
O2W-Er1-O63	137.4(3)	O6W-Er2-O4W	141.2(3)
O2W-Er1-O3W	76.0(3)	O6W-Er2-O5W	72.7(4)
O2W-Er1-O8W	74.9(3)	O30-Er3-O33	77.7(3)
O3W-Er1-O28	73.9(3)	O30-Er3-O68	141.9(3)
O3W-Er1-O63	73.1(3)	O30-Er3-O72	78.9(3)
O3W-Er1-O8W	139.7(3)	O30-Er3-O1W	119.8(3)
O8W-Er1-O28	121.2(2)	O30-Er3-O7W	83.6(3)
O3W-Er1-O63	112.8(2)	O30-Er3-O8W	140.4(3)
O27-Er2-O32	75.7(3)	O30-Er3-O9W	71.3(3)
O27-Er2-O62	143.7(3)	O33-Er3-O68	135.0(3)
O27-Er2-O63	140.4(3)	O33-Er3-O72	81.0(3)
O27-Er2-O1W	120.2(3)	O33-Er3-O1W	69.9(3)
O27-Er2-O4W	74.2(3)	O33-Er3-O7W	149.9(3)
O27-Er2-O5W	73.6(3)	O33-Er3-O8W	69.9(3)
O27-Er2-O6W	79.4(3)	O33-Er3-O9W	115.7(3)
O32-Er2-O62	140.5(3)	O68-Er3-O72	119.2(3)
O32-Er2-O63	72.6(3)	O68-Er3-O1W	70.1(2)
O32-Er2-O1W	72.1(3)	O68-Er3-O7W	72.4(3)
O32-Er2-O4W	115.1(3)	O68-Er3-O8W	77.4(3)
O32-Er2-O5W	144.5(3)	O68-Er3-O9W	75.5(3)
O32-Er2-O6W	84.5(3)	O72-Er3-O1W	139.3(3)
O62-Er2-O63	71.9(3)	O72-Er3-O7W	72.4(3)
O62-Er2-O1W	80.3(3)	O72-Er3-O8W	74.2(3)
O62-Er2-O4W	83.7(3)	O72-Er3-O9W	140.7(3)
O62-Er2-O5W	72.5(3)	O7W-Er3-O1W	140.3(3)
O62-Er2-O6W	102.4(3)	O7W-Er3-O8W	114.3(3)
O1W-Er2-O63	71.1(3)	O8W-Er3-O1W	69.5(3)
O1W-Er2-O5W	140.3(3)	O9W-Er3-O1W	79.1(3)
O4W-Er2-O63	141.6(3)	O8W-Er3-O7W	79.3(3)
O4W-Er2-O1W	76.0(3)	O8W-Er3-O8W	143.9(3)
O4W-Er2-O5W	72.8(3)	Er1-O42-Er2	102.460(15)
O5W-Er2-O63	124.1(3)	Er1-O48-Er3	100.564(14)
O6W-Er2-O63	74.6(3)	Er1-O74-Er3	98.012(13)
O6W-Er2-O1W	142.8(3)		

Table S9 Relaxation fitting parameters from least-squares fitting of $\chi(\omega)$ data of **1**.

T/K	α_1	α_2	$\Delta\chi_1$/cm^3 mol^{-1}	$\Delta\chi_2$/cm^3 mol^{-1}	τ_1/s	τ_2/s	$\chi_{s,tot}$/cm^3 mol^{-1}
2.0	0.16421	0.39146	4.66775	8.76193	2.22884×10^{-4}	0.24782	11.01469
2.1	0.18020	0.38504	4.62245	7.62994	1.81589×10^{-4}	0.19757	10.61995
2.2	0.23469	0.21989	4.97757	4.31230	1.48248×10^{-4}	0.16258	10.16743
2.4	0.2878	0.22097	5.03636	3.30812	1.00191×10^{-4}	0.10621	9.67703
2.6	0.28777	0.27865	4.44723	3.11013	7.99563×10^{-5}	0.08430	9.66670
2.8	0.37304	0.28301	4.05652	2.01895	3.58979×10^{-5}	0.06086	9.14171
3.0	0.42971	0.18214	6.29960	1.61919	2.33217×10^{-5}	0.04121	7.511220
3.2	0.45949	0.23169	5.38050	1.32714	9.37751×10^{-6}	0.0295	7.35975

Table S10 Calculated and found analyses of As, W, Er and Y in **1**, **2** and **Er@2**.

	sample	**As (%)**	**W (%)**	**Er(%)**	**Y(%)**
calcd	**1**	2.47	57.47	8.26	0
	2	2.56	59.78	0	4.56
	Er@2	2.64	61.58	0.15	1.49
found	**1**	2.23	56.98	8.01	0
	2	2.50	58.87	0	4.36
	Er@2	2.52	60.59	0.13	1.37

Table S11 Relaxation fitting parameters from least-squares fitting of $\chi(\omega)$ data of **Er@2**.

T/K	α	χ_1/cm^3 mol^{-1}	χ_2/cm^3 mol^{-1}
2.0	0.56977	1.88534	0.02301
2.1	0.50005	1.39909	0.06637
2.4	0.52691	1.20601	0.08321
2.8	0.52698	1.00886	0.11625
3.2	0.57032	0.91715	0.11994
3.6	0.59532	0.80576	0.12169

Table S12 Calculated energy levels (cm^{-1}), ***g*** (g_x, g_y, g_z) tensors and predominant m_J values of the lowest eight Kramers doublets (KDs) of individual Er^{3+} fragments for compound **1** using CASSCF/RASSI-SO with MOLCAS 8.4.

KDs	**Er1**			**Er2**			**Er3**		
	E/cm^{-1}	***g***	m_J	E/cm^{-1}	***g***	m_J	E/cm^{-1}	***g***	m_J
1	0.0	0.395 1.191 16.115	±15/2	0.0	0.043 0.062 17.421	±15/2	0.0	0.086 0.148 17.068	±15/2
2	80.3	0.897 2.471 10.879	±5/2	116.6	0.874 1.813 13.345	±13/2	138.8	1.561 2.726 12.392	±13/2
3	117.1	0.922 1.901 10.162	±1/2	161.3	0.015 1.963 12.012	±11/2	207.2	1.093 2.856 9.755	±9/2
4	162.5	1.469 4.315 7.609	±11/2	220.2	0.416 2.881 11.691	±5/2	248.6	7.431 6.609 2.442	±5/2
5	232.3	3.956 4.597 7.758	±9/2	270.8	2.705 5.406 8.505	±9/2	301.5	0.252 3.524 9.834	±11/2
6	265.2	0.450 1.191 14.765	±13/2	327.5	1.181 1.984 10.632	±7/2	346.5	1.805 3.368 9.362	±7/2
7	309.6	0.483 0.890 13.740	±7/2	422.2	0.174 0.247 13.294	±3/2	472.2	0.491 0.618 13.148	±3/2
8	463.1	0.044 0.084 17.138	±3/2	529.0	0.027 0.051 16.770	±1/2	605.9	0.000 0.056 16.523	±1/2

Table S13. Wave functions with definite projection of the total moment | m_J > for the lowest one or two KDs of individual Er^{3+} fragments from compound **1**.

	E/cm^{-1}	wave functions
Er1	0.0	70.8%|±15/2>+21.7%|±11/2>
	80.3	18.8%|±7/2>+18.6%|±9/2>+16.8%|±5/2>+15.2%|±3/2>+15.0%|±1/2>+11.1%|±13/2>
Er2	0.0	91.4%|±15/2>+5.1%|±11/2>
	116.6	62.1%|±13/2>+16.0%|±7/2>+8.6%|±5/2>+8.3%|±9/2>

Er3	0.0	86.7%|±15/2>+10.8%|±11/2>
	138.8	57.7%|±13/2>+10.7%|±9/2>+9.3%|±7/2>+7.3%|±5/2>+5.4%|±1/2>+4.9%|±3/2>

Table S14. Exchange energies E (cm^{-1}), the energy difference between each exchange doublets Δ_t (cm^{-1}) and the main values of the g_z for the lowest four exchange doublets of $\{Er_3\}$ fragment in **1**.

	1		
	E	Δ_t	g_z
1	0.0	0.3×10^{-11}	29.318
2	0.3	0.1×10^{-11}	21.703
3	2.5	0.1×10^{-11}	22.833
4	4.9	0.1×10^{-11}	34.080

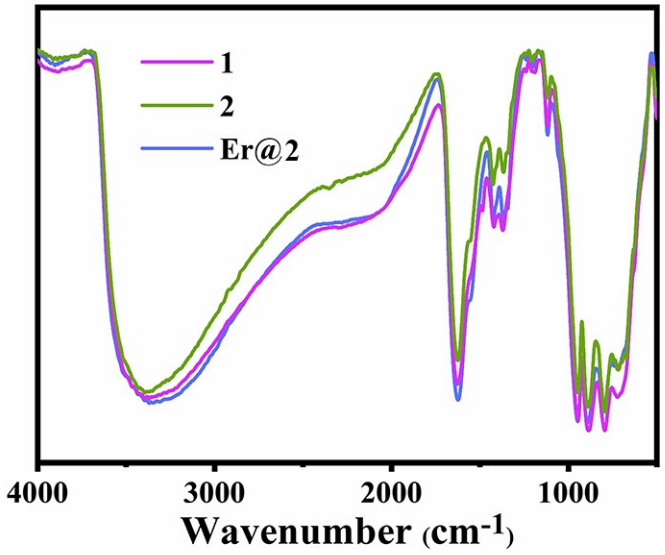

Fig. S1. IR spectra of **1**, **2** and **Er@2**, respectively.

IR spectra of all compounds have been conducted on a Nicolet 170 SXFT–IR spectrometer in the range of 400–4000 cm^{-1} with KBr pellets, which are all very similar with only slight shifts in the position of the bands (Fig. S1). In their high wave-number region, a significant widen obvious broad band in the range of 3400–1623 cm^{-1} which are attributed to the stretching vibration ν(O–H) and bending vibration δ(O–H) of free modes of lattice and coordinated water

molecules, respectively. Due to the existence of the trivacant Keggin $[B\text{-}\alpha\text{-}AsW_9O_{33}]^{9-}$ fragments in the skeletons of the three compounds, **1** shows bands in the region 1000–400 cm^{-1}, which correspond to the fingerprint region. In the low wave-number region, four characteristic peaks are seen, which are respectively explained by the asymmetric vibrations of the terminal $\nu(W–O_t)$, corner-sharing $\nu(W–O_b)$ and $\nu(As–O_a)$, and edge-sharing $\nu(W–O_c)$ bonds. The strong peak at 948 cm^{-1} is due to the $\nu(W–O_t)$ bond and the intense peak at 864 cm^{-1} is due to an $\nu(W–O_b)$ bond. Two medium intensity peaks at 789 and 718 cm^{-1} are due to $\nu(As–O_a)$ and $\nu(W–O_c)$ bonds. In addition, in comparison with uncoordinated carboxylate acid (about 1700 cm^{-1}), the band at 1630 cm^{-1} is assigned to COO^- stretching vibrations from the carboxylate of the monodentate-coordinated mal carboxylate ligands.

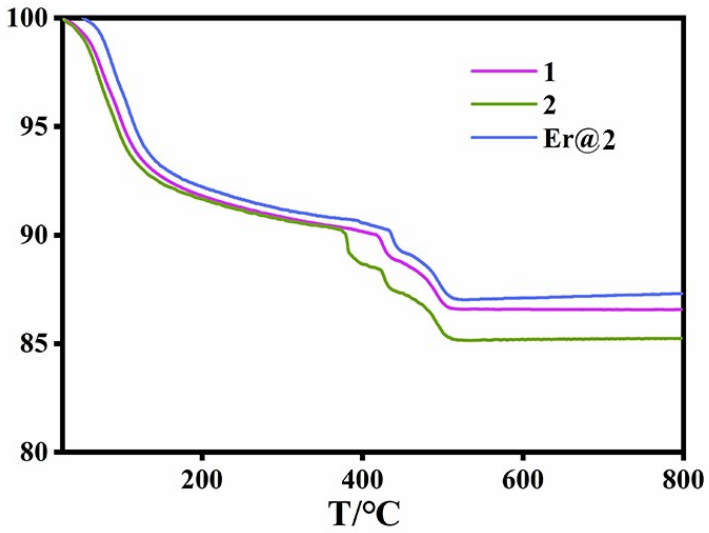

Fig. S2. Thermogravimetric curves of **1, 2 and Er@2**.

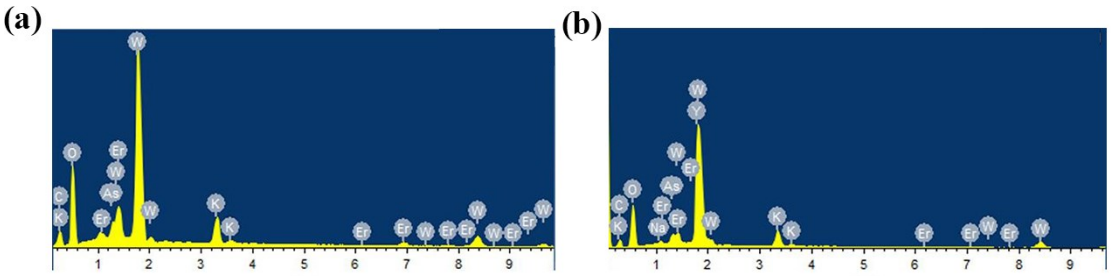

Fig. S3. EDX spectra of **1** and **Er@2** showing the presence of C, O, As, K, W, Er and Y element in the lattice. The measured ratios of Er^{3+}/ Y^{3+} ions are almost consistent with nominal ratios.

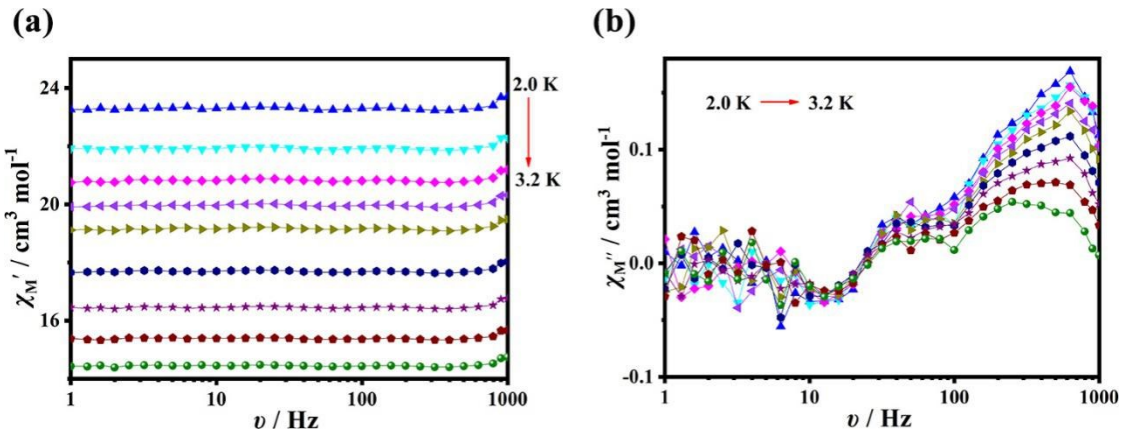

Fig. S4. Frequency dependence of the in-phase (χ_M') and out-of-phase (χ_M'') products under a zero dc field for **1**.

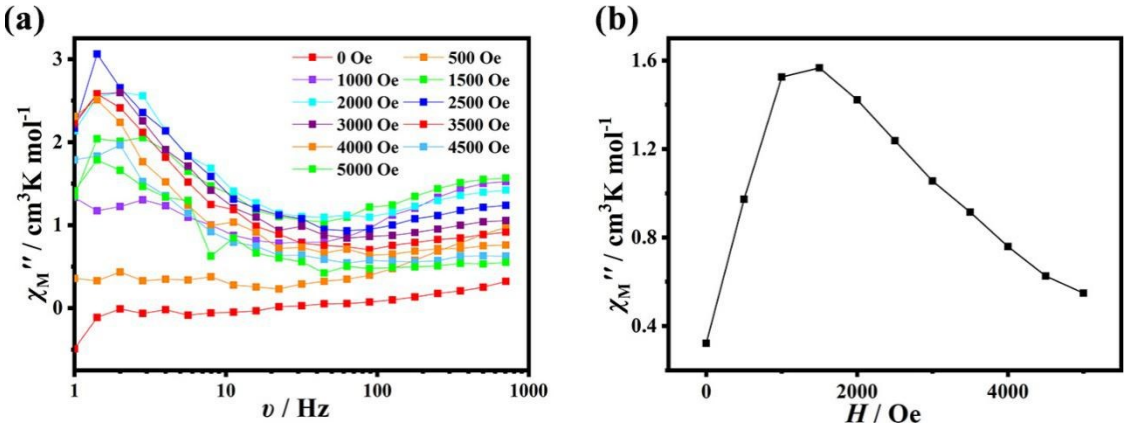

Fig. S5. At 2.0 K, sweep field diagram of **1** from 0 to 5000 Oe, and the optimal dc field was determined to be 1500 Oe at 2.0 K, 707.2Hz.

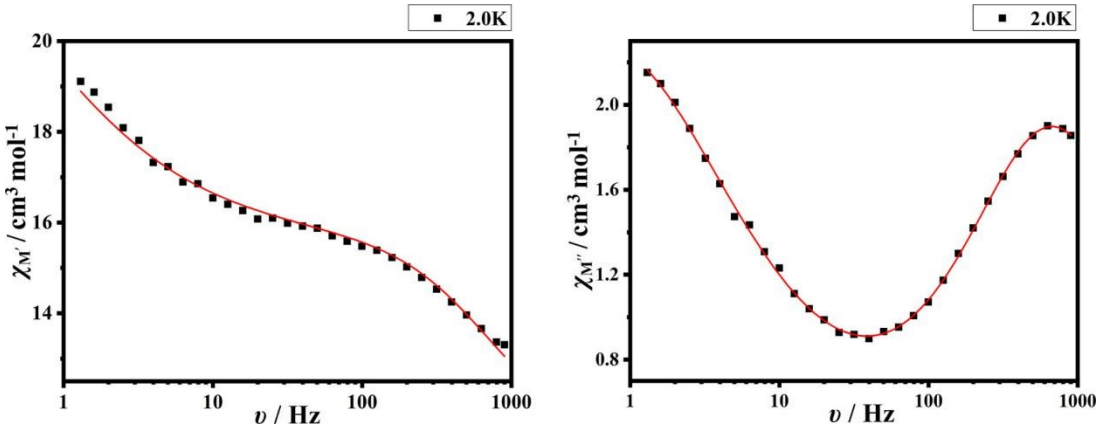

Fig. S6. At 2.0 K, the real part (left) and imaginary part (right) of compound **1** ac signal frequency dependence diagram, solid line represents Debye model fitting curve, fitting parameters: α_1= 0.16421; α_2= 0.39146; τ_1= 2.22884×10^{-4} s; τ_2= 0.24782 s; $\chi_{s,tot}$= 11.01469 cm^3 mol^{-1}; $\Delta\chi_1$= 4.66775 cm^3 mol^{-1}; $\Delta\chi_2$= 8.76193 cm^3 mol^{-1}.

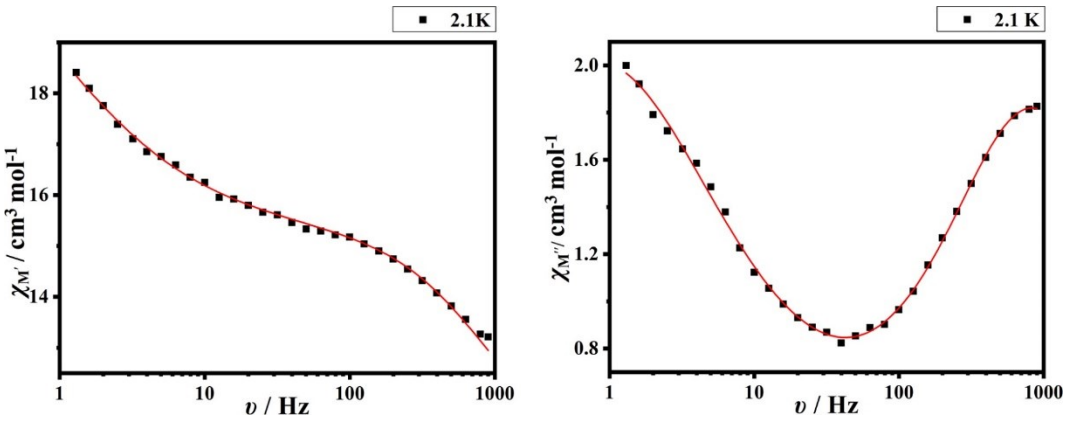

Fig. S7. At 2.1 K, the real part (left) and imaginary part (right) of compound **1** ac signal frequency dependence diagram, solid line represents Debye model fitting curve, fitting parameters: α_1= 0.18020; α_2= 0.38504; τ_1= 1.81589×10^{-4} s; τ_2= 0.19757 s; $\chi_{s,tot}$= 10.61995 cm^3 mol^{-1}; $\Delta\chi_1$= 4.62245 cm^3 mol^{-1}; $\Delta\chi_2$= 7.62994 cm^3 mol^{-1}.

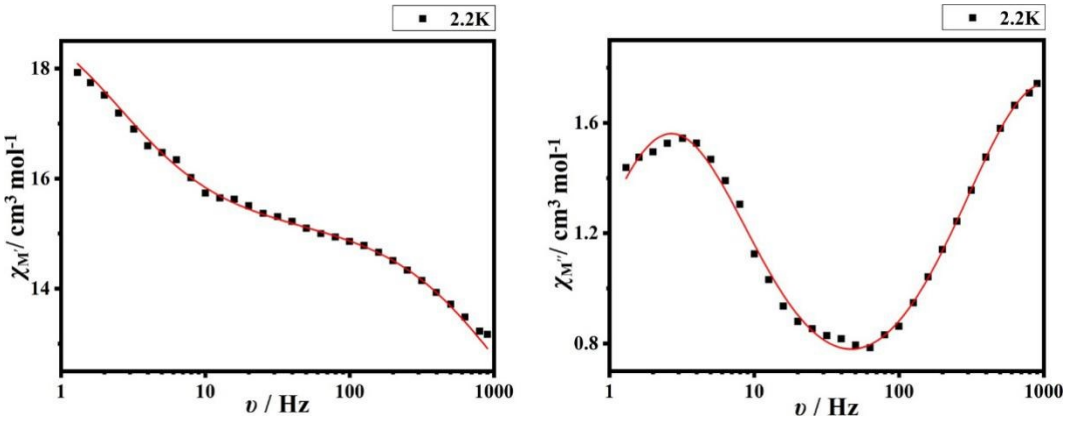

Fig. S8. At 2.2 K, the real part (left) and imaginary part (right) of compound **1** ac signal frequency dependence diagram, solid line represents Debye model fitting curve, fitting parameters: α_1= 0.23469; α_2= 0.21989; τ_1= 1.48248×10^{-4} s; τ_2= 0.16258 s; $\chi_{s,tot}$= 10.16743 cm^3 mol^{-1}; $\Delta\chi_1$= 4.97757 cm^3 mol^{-1}; $\Delta\chi_2$= 4.31230 cm^3 mol^{-1}.

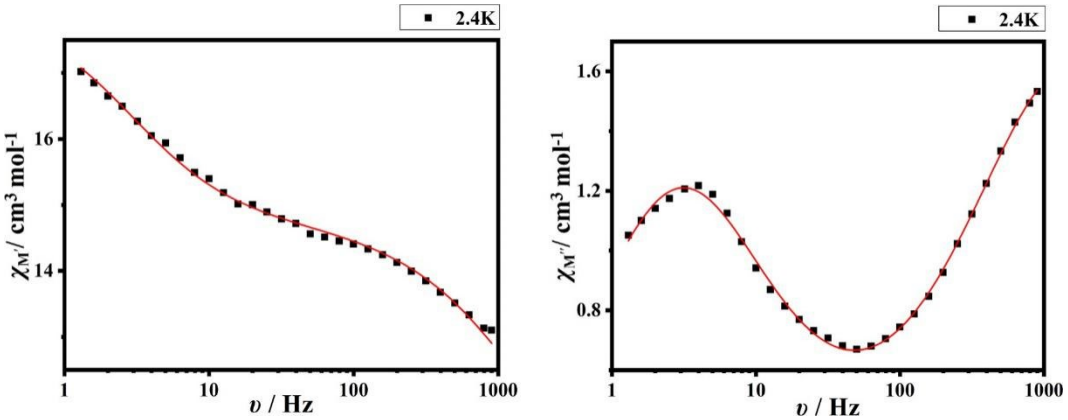

Fig. S9. At 2.4 K, the real part (left) and imaginary part (right) of complex **1** ac signal frequency dependence diagram, solid line represents Debye model fitting curve, fitting parameters: α_1=0.2878; α_2= 0.22097; τ_1= 1.00191×10^{-4} s; τ_2= 0.10621 s; $\chi_{s,tot}$= 9.67703 cm^3 mol^{-1}; $\Delta\chi_1$= 5.03636 cm^3 mol^{-1}; $\Delta\chi_2$= 3.30812 cm^3 mol^{-1}.

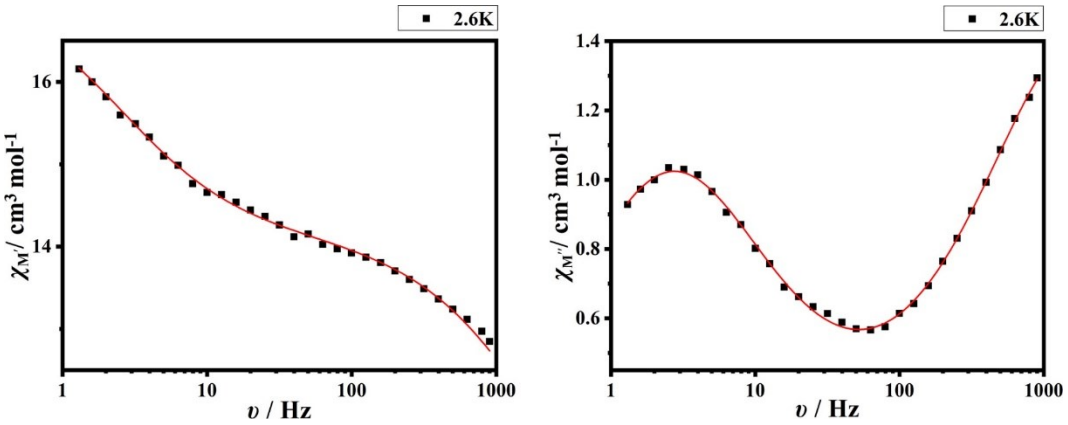

Fig. S10. At 2.6 K, the real part (left) and imaginary part (right) of compound **1** ac signal frequency dependence diagram, solid line represents Debye model fitting curve, fitting parameters: α_1= 0.28777; α_2= 0.27865; τ_1= 7.99563×10^{-5} s; τ_2= 0.08430 s; $\chi_{s,tot}$= 9.66670 cm^3 mol^{-1}; $\Delta\chi_1$= 4.44723 cm^3 mol^{-1}; $\Delta\chi_2$= 3.11013 cm^3 mol^{-1}.

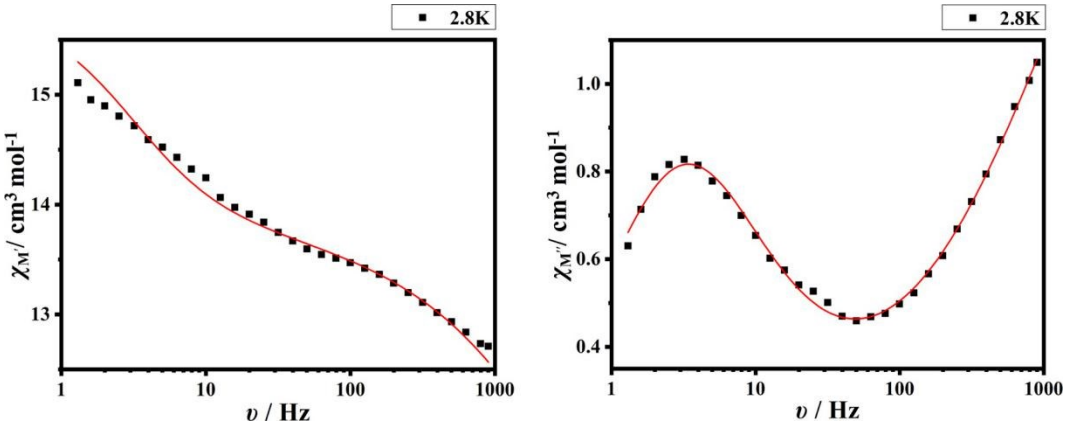

Fig. S11. At 2.8 K, the real part (left) and imaginary part (right) of compound **1** ac signal frequency dependence diagram, solid line represents Debye model fitting curve, fitting parameters: α_1= 0.37304; α_2= 0.28301; τ_1= 3.58979×10^{-5} s; τ_2= 0.06086 s; $\chi_{s,tot}$= 9.14171 cm^3 mol^{-1}; $\Delta\chi_1$= 4.05652 cm^3 mol^{-1}; $\Delta\chi_2$= 2.01895 cm^3 mol^{-1}.

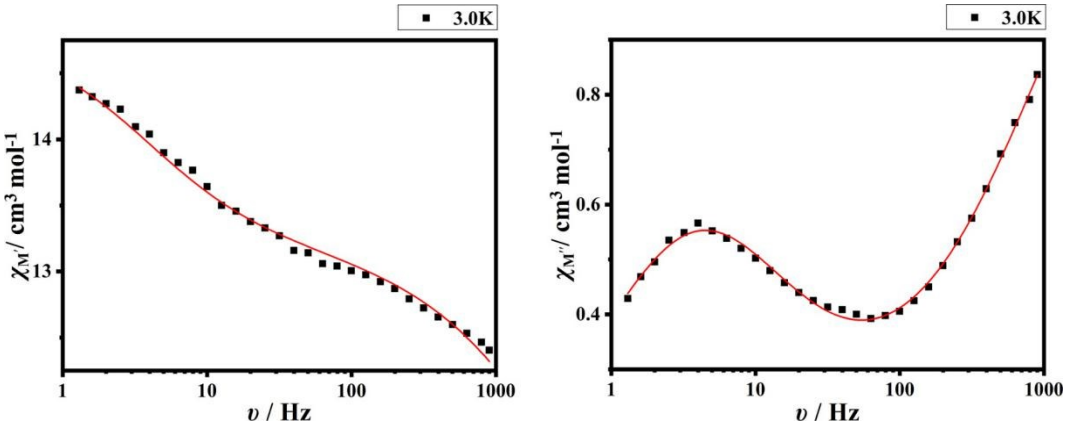

Fig. S12. At 3.0 K, the real part (left) and imaginary part (right) of compound **1** ac signal frequency dependence diagram, solid line represents Debye model fitting curve, fitting parameters: α_1= 0.42971; α_2= 0.18214; τ_1= 2.33217×10^{-5} s; τ_2= 0.04121 s; $\chi_{s,tot}$= 7.511220 cm^3 mol^{-1}; $\Delta\chi_1$= 6.29960 cm^3 mol^{-1}; $\Delta\chi_2$= 1.61919 cm^3 mol^{-1}.

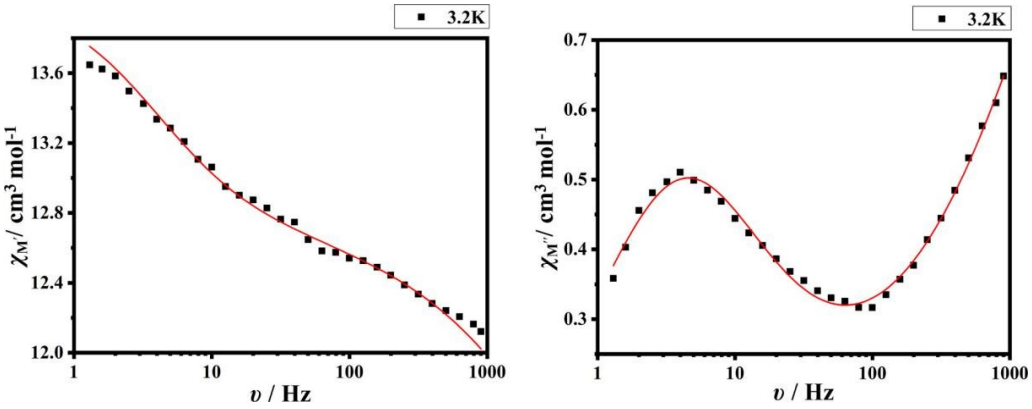

Fig. S13. At 3.2 K, the real part (left) and imaginary part (right) of compound **1** ac signal frequency dependence diagram, solid line represents Debye model fitting curve, fitting parameters: α_1= 0.45949; α_2= 0.23169; τ_1= 9.37751×10^{-6} s; τ_2= 0.0295 s; $\chi_{s,tot}$= 7.35975 cm^3 mol^{-1}; $\Delta\chi_1$= 5.3805 cm^3 mol^{-1}; $\Delta\chi_2$= 1.32714 cm^3 mol^{-1}. The magnetic susceptibility data were described by the sum of two modified Debye functions:

$$\chi''(\omega)=\Delta\chi_1\frac{(\omega\tau_1)^{1-\alpha_1}\cos(\pi\alpha_1/2)}{1+2(\omega\tau_1)^{1-\alpha_1}\sin(\pi\alpha_1/2)+(\omega\tau_1)^{(2-2\alpha_1)}}+\Delta\chi_2\frac{(\omega\tau_2)^{1-\alpha_2}\cos(\pi\alpha_2/2)}{1+2(\omega\tau_2)^{1-\alpha_2}\sin(\pi\alpha_2/2)+(\omega\tau_2)^{(2-2\alpha_2)}}$$

$\Delta\chi_1$, τ_1, α_1, $\Delta\chi_2$, τ_2, α_2

$$\chi'(\omega)=\chi_{s,tot}+\Delta\chi_1\frac{1+(\omega\tau_1)^{1-\alpha_1}\sin(\pi\alpha_1/2)}{1+2(\omega\tau_1)^{1-\alpha_1}\sin(\pi\alpha_1/2)+(\omega\tau_1)^{(2-2\alpha_1)}}+\Delta\chi_2\frac{1+(\omega\tau_2)^{1-\alpha_2}\sin(\pi\alpha_2/2)}{1+2(\omega\tau_2)^{1-\alpha_2}\sin(\pi\alpha_2/2)+(\omega\tau_2)^{(2-2\alpha_2)}}$$

$\chi_{s,tot}$, $\Delta\chi_1$, τ_1, α_1, $\Delta\chi_2$, τ_2, α_2

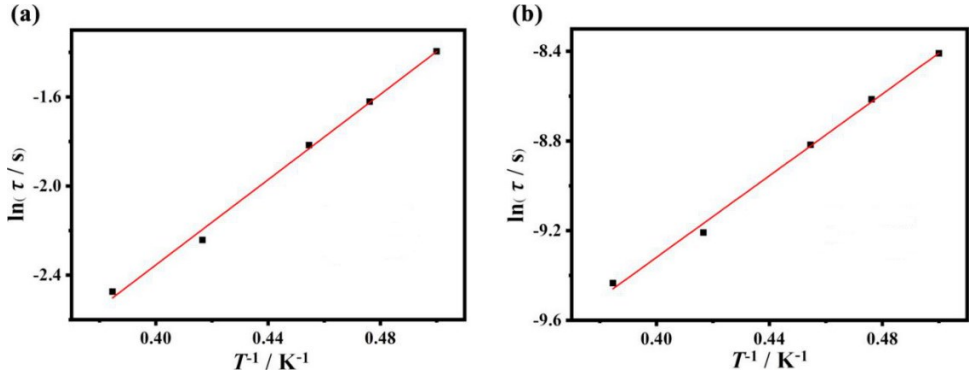

Fig. S14. Plot of ln(τ/s) versus T^{-1} for compound **1** under 1500 dc field. Left: FR process, right: SR process.

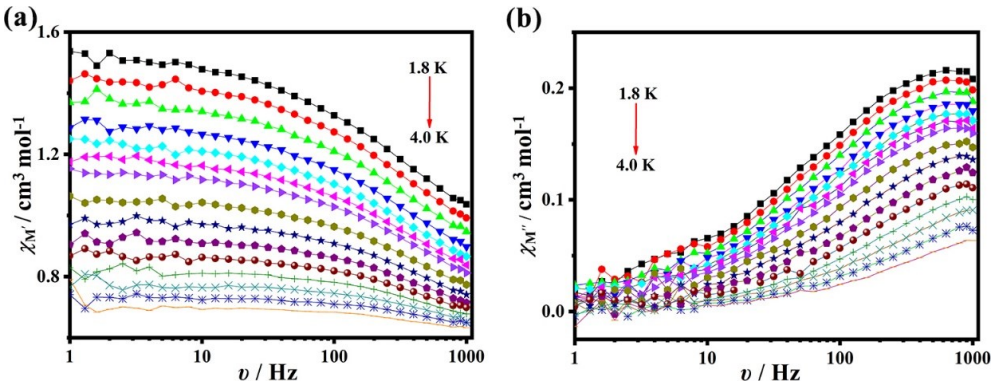

Fig. S15. Frequency dependence of the in-phase (χ'_M) and out-of-phase (χ''_M) products under a zero dc field for **Er@2**.

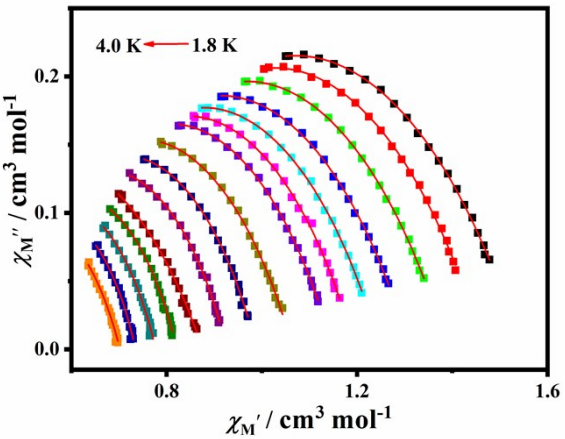

Fig. S16. Cole–Cole plot under a zero dc field for **Er@2** at the indicated temperatures. The lines are guides to the eyes.

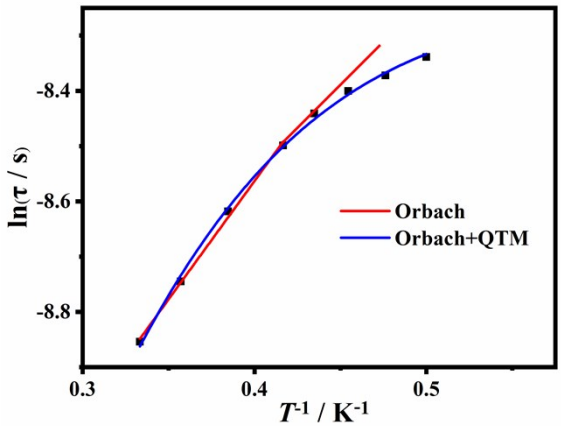

Fig. S17. Plot of ln(τ/s) versus T^{-1} of **Er@2** under a zero dc field with fitting results.

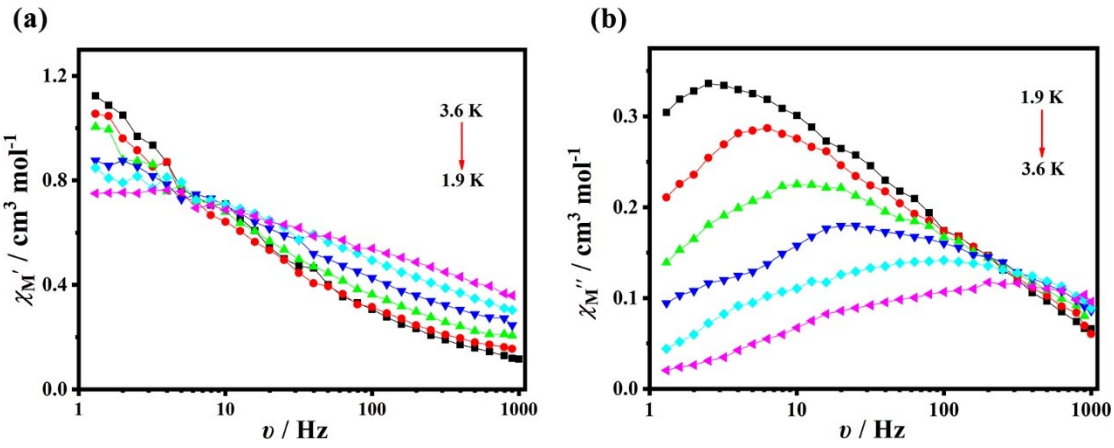

Fig. S18. Frequency dependence of the in-phase (χ_M') and out-of-phase (χ_M'') products under an optimized 1500 Oe dc field for **Er@2**. The lines are guides to the eyes.

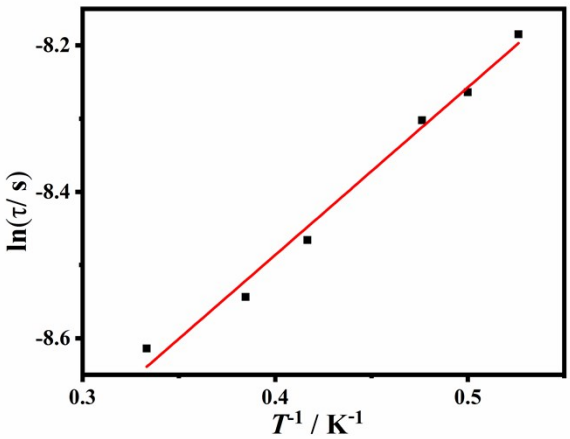

Fig. S19. plot of ln(τ/*s*) versus T^{-1} for compound **Er@2** under 1500 dc field.

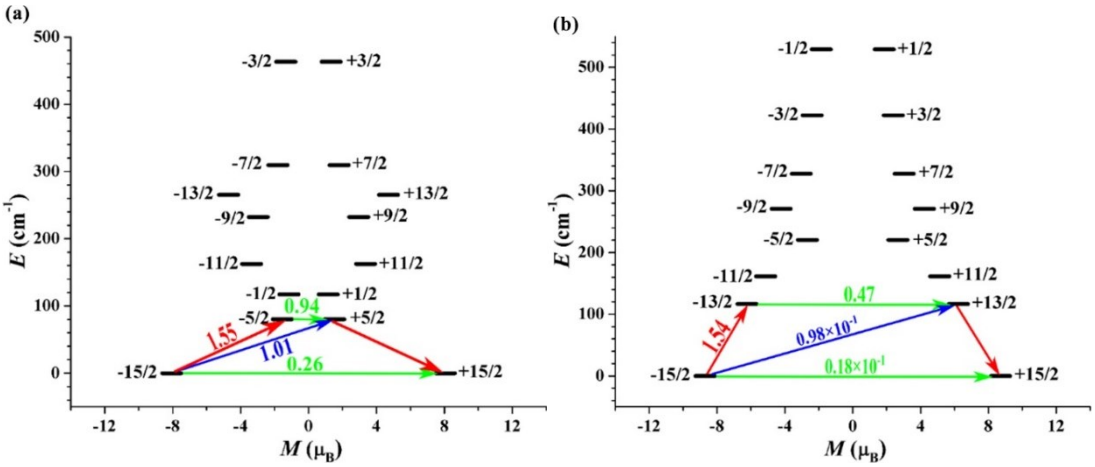

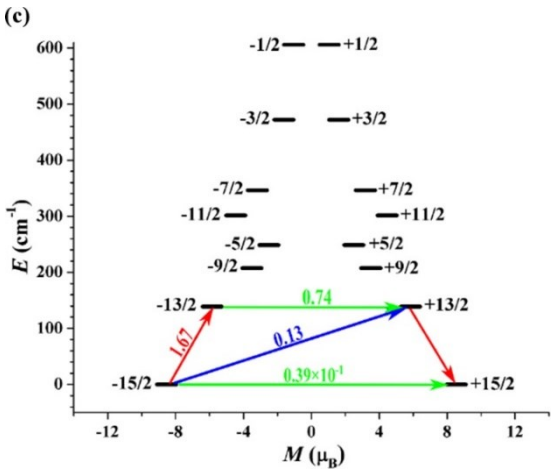

Fig. S20. Magnetization blocking barriers of individual Er^{3+} fragments from compound **1**: (a) Er1, (b) Er2 and (c) Er3. The thick black lines represent the KDs as a function of their magnetic moment along the magnetic axis. The green lines correspond to diagonal quantum tunneling of magnetization (QTM); the blue line represent off-diagonal relaxation process. The path shown by the red arrows represents the most probable path for magnetic relaxation in the corresponding compounds. The numbers at each arrow stand for the mean absolute value of the corresponding matrix element of transition magnetic moment.

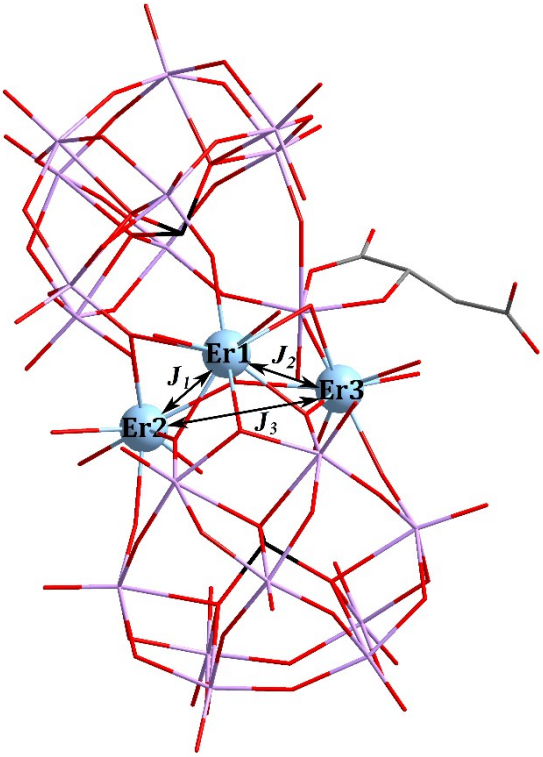

Fig. S21. Scheme of the Er^{3+}-Er^{3+} interactions in compound **1**.

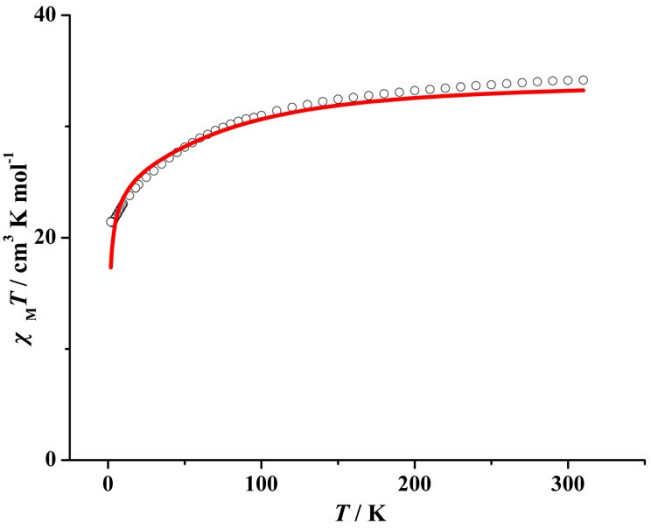

Fig. S22. Calculated (red solid line) and experimental (white circle) data of magnetic susceptibility of $\{Er_3\}$ fragment in **1**. The intermolecular interaction zJ' of $\{Er_3\}$ fragment in **1** was fitted to -0.16 cm^{-1}.

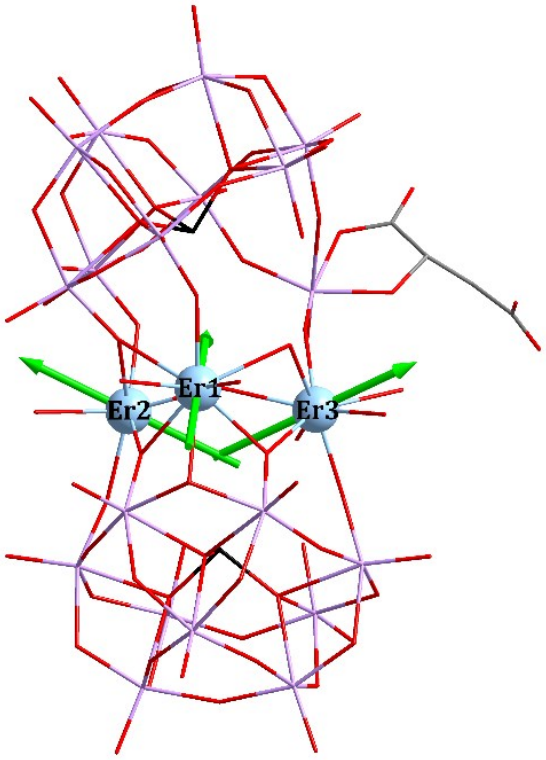

Fig. S23. Calculated orientations of the local main magnetic axes on Er^{3+} ions of $\{Er_3\}$ fragment in **1** in the ground KDs.

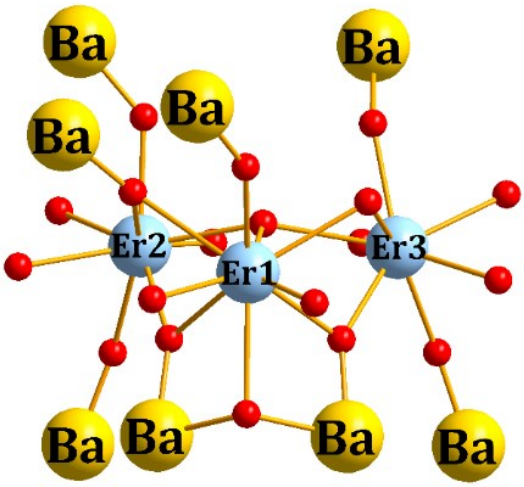

Fig. S24. Calculated model structures of individual Er^{3+} fragments in **1**; H atoms are omitted for clarify.

References:

S1 U. Kortz, M. G. Savelieff, B. S. Bassil and M. H. Dickman, *Angew. Chem., Int. Ed.*, 2001, **40**, 3384–3386.

S2 Sheldrick, G. M. Crystal Structure Refinement with SHELXL. *Acta Crystallogr., Sect. C: Struct. Chem.* 2015, **71**, 3–8.

S3 F. Aquilante, J. Autschbach, R. K. Carlson, L. F. Chibotaru, M. G. Delcey, L. De Vico, I. Fdez. Galván, N. Ferré, L. M. Frutos, L. Gagliardi, M. Garavelli, A. Giussani, C. E. Hoyer, G. Li Manni, H. Lischka, D. Ma, P. Å. Malmqvist, T. Müller, A. Nenov, M. Olivucci, T. B. Pedersen, D. Peng, F. Plasser, B. Pritchard, M. Reiher, I. Rivalta, I. Schapiro, J. Segarra-Martí, M. Stenrup, D. G. Truhlar, L. Ungur, A. Valentini, S. Vancoillie, V. Veryazov, V. P. Vysotskiy, O. Weingart, F. Zapata, R. Lindh, MOLCAS 8: New Capabilities for Multiconfigurational Quantum Chemical Calculations across the Periodic Table, *J. Comput. Chem*., 2016, **37**, 506−541.

S4 Seijo, L.; Barandiarán, Z. *Computational Chemistry: Reviews of Current Trends*; World Scientific, Inc.: Singapore, 1999; pp 455−152.

S5 (a) Chibotaru, L. F.; Ungur, L.; Soncini, A. *Angew. Chem. Int. Ed.*, 2008, **47**, 4126−4129. (b) Ungur, L.; Van den Heuvel, W.; Chibotaru, L. F. *New J. Chem.*, 2009, **33,** 1224−1230. (c) Chibotaru, L. F.; Ungur, L.; Aronica, C.; Elmoll, H.; Pilet, G.; Luneau, D. *J. Am. Chem. Soc.*, 2008, **130**, 12445−12455.

S6 Lines, M. E. *J. Chem. Phys*. 1971, **55**, 2977.

S7 (a) Mondal, K. C.; Sundt, A.; Lan, Y. H.; Kostakis, G. E.; Waldmann, O.; Ungur, L.; Chibotaru, L. F.; Anson, C. E.; Powell, A. K. *Angew. Chem. Int. Ed*. 2012, **51**, 7550−7554. (b) Langley, S.

K.; Wielechowski, D. P.; Vieru, V.; Chilton, N. F.; Moubaraki, B.; Abrahams, B. F.; Chibotaru, L. F.; Murray, K. S. *Angew. Chem. Int. Ed*. 2013, **52**, 12014−12019.